KSCE Journal of Civil Engineering (2020) 24(1):228-240
DOI 10.1007/s12205-020-0888-2

pISSN 1226-7988, eISSN 1976-3808
www.springer.com/12205

Structural Engineering

The Mechanical Properties of a New Corrugated Steel Plate Damper and Its Application in a Steel Arch Bridge

Weining Sui[a], Hang Li[b], Qiang Zhang[b], Zhanfei Wang[b], and Xiayu Jin[c]

[a]*School of Civil Engineering, Shenyang Jianzhu University, Shenyang 110168, China*
[b]*School of Transportation Engineering, Shenyang Jianzhu University, Shenyang 110168, China*
[c]*Capital Engineering & Research Incorporation Limited Guangdong Branch, Guangzhou 510220, China*

ARTICLE HISTORY

Received 23 May 2019
Revised 26 September 2019
Accepted 16 October 2019
Published Online 29 November 2019

KEYWORDS

Corrugated steel plate damper
Mechanical properties
Seismic performance
Arch bridge
Dynamic time history analysis

ABSTRACT

An innovative application of a new corrugated steel plate damper (CSPD) in steel arch bridges is proposed to enhance their seismic performance. The mechanical properties of the CSPD were investigated by static and quasi-static parametric analysis using ABAQUS software, and validation of the CSPD finite element models was conducted by comparing the numerical results with published experimental results. The results indicate that the CSPD has desirable mechanical properties and hysteretic performance when the geometric design parameters lie within a reasonable range. Then a selected CSPD with reasonable geometric design parameters was installed on the side piers of upper-deck type steel truss arch bridge to explore the resulting improvement in the seismic behaviour of the original arch bridge. The displacement and force responses indicate that the selected CSPD can improve energy dissipation and the seismic behaviour of the arch bridge in transverse and longitudinal directions in major earthquakes.

1. Introduction

Bridges designed according to the traditional seismic design method suffered significant damage or even collapse during major earthquake events (Bruneau, 1998; Du et al., 2008; Wang et al., 2012), which indicates that the traditional seismic method is not sufficient to meet seismic design requirements in regions of high seismic intensity. In the last few years, isolator devices and energy dissipation restrainers, such as steel plate shear walls, buckling-restrained braces, lead rubber bearings etc., have been applied to meet new seismic design requirements (Iemura, 2012).

In recent years, steel plate shear walls have been widely used in the structures as a lateral load-resisting system (EN 1993-1-5 Eurocode 3, 2005; CSA, 2009; AISC 341-10, 2010). Shear steel plate dampers (SSPD) are developed in 1990s and mainly comprise three parts: a web, left and right flange plates, and, upper and lower end connection plates. The dampers can be used as an economical and effective energy dissipation device in buildings and bridges through the elasto-plastic shear deformation of the steel web. Nakashima and other collaborators first studied the strain-hardening behaviour of shear plates made of low-yield steel through experiment and simulation methods (Nakashima, 1995; Nakashima et al., 1995). The results showed that the SSPD offers good hysteresis performance. Researchers also have studied the static, hysteretic, and dynamic behaviour of the SSPD (Tanaka and Sasaki, 2000; Usami et al., 2000; Chen et al., 2006; Zhang et al., 2012; Xu et al., 2017), and considered the influence of design parameters on the hysteretic behaviour of the SSPD. The results indicate that the parameters, including the web width to thickness ratio, strength of the web steel, stiffener arrangement, and number of stiffeners, affect the hysteretic behaviour and failure mode of the SSPD. The welded flange on the web can enhance the stability of the shear plate, but the weld toe between the web and the flange forms a weak part of the shear steel plate damper, which will be damaged before the web during an earthquake and result in an overall failure. Comparing with conventional flat steel plate, the corrugated steel plates show higher out of plane stiffness, in-plane shear strength, and elastic buckling capacity. Through experiment and simulation analysis, these results indicated that corrugated steel plates had good mechanical properties (Ichioka et al., 2009; Qiu et al., 2018; Dou et al., 2018). Yi J carried out a theoretical study of the

CORRESPONDENCE Zhanfei Wang ✉ ZFWang@sjzu.edu.cn School of Transportation Engineering, Shenyang Jianzhu University, Shenyang 110168, China

buckling behaviour of corrugated steel plate, which shows how geometric parameters affect shear buckling modes and proposes an interactive shear buckling strength formula (Yi et al., 2008). It is reported that finite element analysis modelling can predict the structural strength of the corrugated models as well as the failure modes (Kumar et al., 2013; Kalali et al., 2016; Chaubey et al., 2018a; Chaubey et al., 2018b; Anish et al., 2019a; Anish et al., 2019b; Anish et al., 2019c; Ansari et al., 2019).

Currently, the corrugated webs have been mostly used as the web of girder bridges in practical applications. Researchers have studied the mechanical behaviour of bridge girders with corrugated web plates using the experimental and finite element analysis methods (Machimdamrong et al., 2004; Ibrahim et al., 2006; Ezzeldin, 2007; Abbas et al., 2007a; Abbas et al., 2007b; Jáger et al., 2015; Elkawas et al., 2017; Farhad et al., 2018). It is found that use of corrugated steel plate as the web can improve the stiffness and ductility of girder components. Wang used corrugated steel plates instead of concrete webs in a crossbeam in the tower of a suspension bridge (Wang et al., 2019). The experimental results show that the energy dissipation capacity of such a composite beam is better than that of the RC structures, the strength degradation is slight when the specimen has an appropriate shear-span ratio, and the deformation recovery ability is good for all test specimens. Asynchronous construction, a new construction method for composite girder bridges with corrugated steel webs, has also been introduced (Deng et al., 2019).

In this paper, considering the virtues of corrugated plate, such as larger shear capacity, smaller width to thickness ratio as a web, and the excellent out-of-plane stability, a new corrugated steel plate damper (CSPD) is proposed to eliminate weakness at the weld between the web and flange. To promote the use of corrugated steel plates as dampers for improving the seismic performance of bridges or buildings, 25 finite element models of corrugated plates were established using the elasto-plastic analysis software ABAQUS, to investigate its mechanical properties. Static and quasi-static analyses were performed to explore the effects of five main geometric design parameters (ripple angle θ, width to thickness ratio of corrugated webs a_2/t_w, the number of corrugations n, height to width ratio of the corrugated web H/B, and the ratio of the slanting plate segment to the straight plate segment a_1/a_2) on the mechanical properties and hysteresis behaviour of the corrugated steel plate. Then a selected CSPD was applied to an upper-deck type steel truss arch bridge, and dynamic time history analysis was performed to study its effect on the seismic performance of arch bridges.

2. The Corrugated Steel Plate Damper

The corrugated steel plate damper proposed here is composed of a corrugated steel web which is vertically installed to bear the horizontal load, the left and right flange plates to restrain the corner buckling of plate and improve the shear buckling capacity, and the upper and lower flange plates. The structural configurations and geometric parameters of the corrugated steel plate damper is as shown in Fig. 1.

The load is applied to the CSPD in the horizontal direction and the loading condition is assumed to generate pure shear. According to the Von Mises yield criterion Eq. (1), under pure shear loading conditions, the shear yield force, and yield displacement of the CSPD are given by Eqs. (2) and (3), respectively.

$$\left[(\sigma_1-\sigma_2)^2+(\sigma_2-\sigma_3)^2+(\sigma_3-\sigma_1)^2\right]=6\tau_{\mathrm{y}}{}^2=2\sigma_{\mathrm{y}}^2 \tag{1}$$

$$F_{\mathrm{y}}=\frac{\sigma_y A}{\sqrt{3}} \tag{2}$$

$$\delta_{\mathrm{y}}=\frac{\kappa\times F_y\times H}{GA} \tag{3}$$

where τ_y is the shear yield strength of steel; σ_y represents the yield strength of steel; F_y is the shear yield force; A indicates the cross-sectional area of the corrugated web; δ_y is the yield shear displacement; H is the height of the corrugated web; G is the shear modulus, and k is the coefficient of the shear deformation ($k = A_1/A_2$). The A_1 is the total cross-sectional area of the left flange, the right flange and the corrugated web. The A_2 is the cross-sectional area of the corrugated web.

3. Validation of Finite Element Models

To ensure the validity and reasonableness of numerical analysis

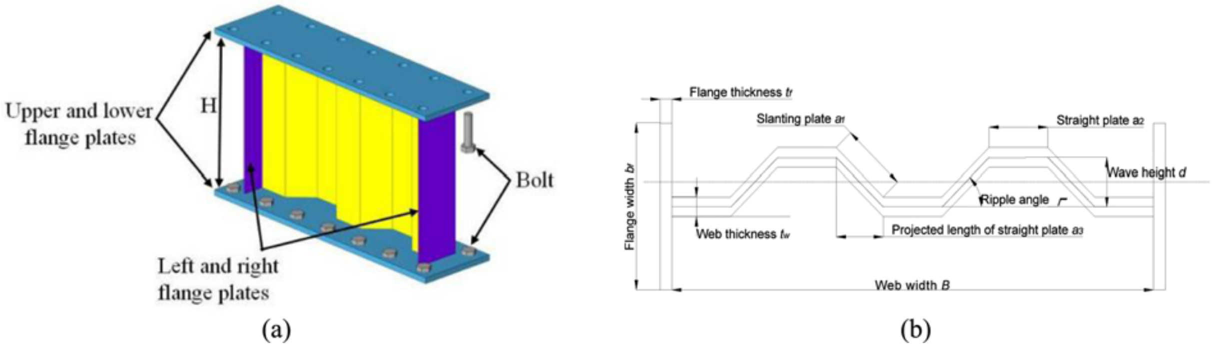

Fig. 1. Corrugated Steel Plate Damper (two ripples): (a) Overall Structure, (b) Top View

model of the CSPD, full-scale simulations according to the experiment (Watanabe and Kubo, 2006; Kubo and Watanabe, 2007) were conducted.

3.1 Experimental Outline

As shown in Fig. 2, the total span of the test specimen is 2400 mm and the total height is 800 mm. A concentrated load was applied by hydraulic jack (capacity 2,000 kN) on a steel plate (120 mm × 18 mm × 260 mm) in the middle of the upper flange plate of the girder with corrugated steel webs. The two bottom ends were connected by pin bolts. To avoid local failure of the corrugated steel web beams under the load position and in the loading process, two stiffener plates (60 mm spacing, 12 mm thickness) were arranged on both sides and in the middle of the beams. To ensure accurate measurement of the deformation of corrugated steel web beams and other test results, the displacement sensors and strain gauges were installed.

Figure 3 shows the geometric parameters of the trapezoidal cross-section of the corrugated steel web beams. The height of corrugated steel web $d_w = 800$ mm, thickness $t_w = 3.2$ mm, width of upper and lower flange $b_f = 200$ mm, thickness of flange $t_f = 12$ mm, which are kept constant for both test specimens. The lengths of the straight section a, the projection length b and the inclined section c of the corrugated steel webs of the two test specimens are summarised in Table 1, in which the length of the straight section is equal to the length c of the inclined section, and the wavelength q of one wave remains constant, i.e. $q = 2a + b = 300$ mm.

The specimens were made of SS400 grade steel according to JIS of Japan, and the material properties were verified by tension testing (Table 2).

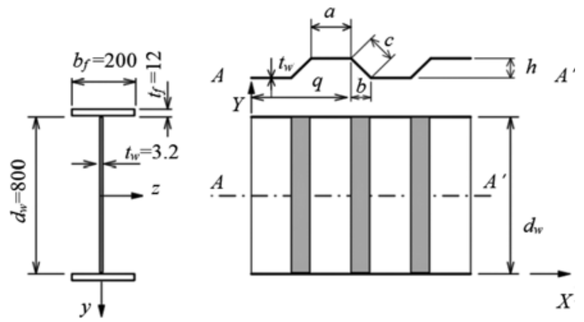

Fig. 3. Section Shape of the Experimental Specimen

Table 1. Size of Corrugated Steel Plate

Test component	h (mm)	a (mm)	b (mm)	c (mm)
CG240-0	0	-	-	-
CG240-6	60	87.0	63.0	87.0

3.2 Finite Element Model of Experimental Specimens

A 3-d full-scale shell model of the experimental specimens is shown in Fig. 4 in the standard module (SIMULIA, 2013). Four-node reduction integration shell element (S4R) was used for the corrugated steel webs, upper and lower flange plates and stiffened ribbed plates, which can ensure the accuracy of analysis and reduce the amount of calculation. The constitutive model for SS400 steel is a bi-linear stress-strain, kinematic hardening model which considers the Bauschinger effect. The secondary stiffness considered as 1/100 of the initial stiffness and the Von Mises yield criterion, was used. Newton-Raphson algorithm was used for elasto-plastic analysis.

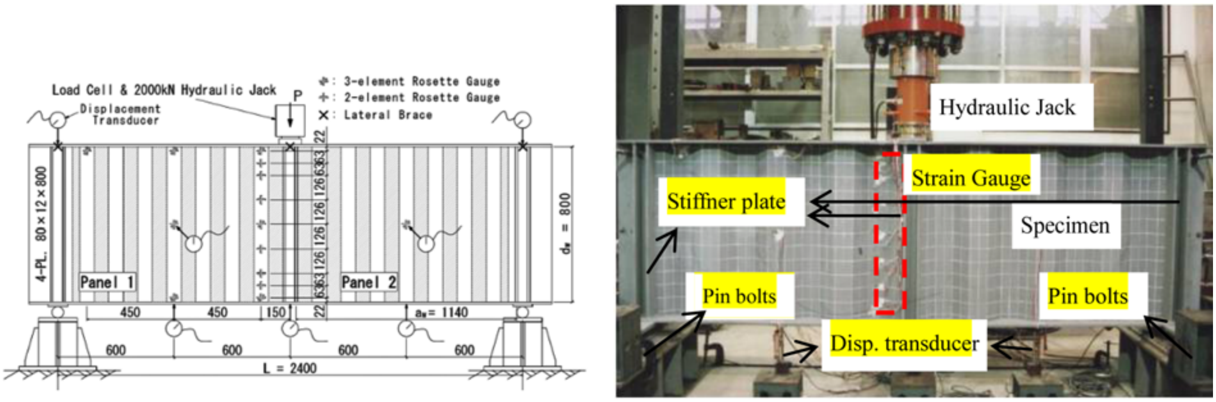

(a) (b)

Fig. 2. Experimental Apparatus: Displacement Transducer and Rosette Gauge Layout: (a) Test Set-Up (elevation), (b) Actual Test Set-Up (elevation)

Table 2. Material Properties

Plate nominal thickness t (mm)	Yield strength σ_y (MPa)	Ultimate strength σ_u (MPa)	Elastic modulus E (GPa)	Poisson's ratio υ	Elongation Δl (%)
3.2 for web	301	425	204	0.279	27.7
12 for flange	255	408	198	0.285	24.6

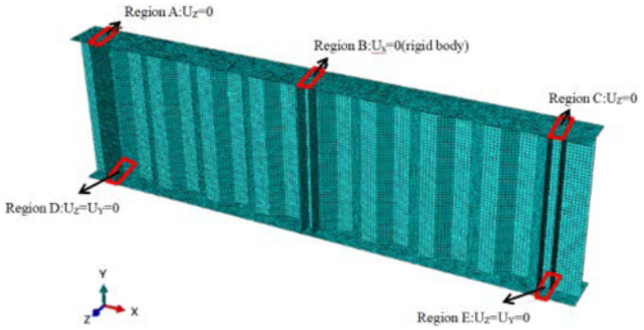

Fig. 4. FE Model of Experimental Specimens

Stiffener ribs were merged with the corrugated plate web, and then corrugated web was combined with the upper and lower flange plates by way of a tie member. The constraint at the loading position was set as a rigid body (Region B). In simulation, a monotonic displacement control protocol was applied at Region B.

3.3 Experimental and Finite Element Analytical Results

The load-displacement curves of the CG240-0 and CG240-6 are depicted in Fig. 5, where the solid line denotes FE analytical results and the dot-solid line denotes the experiment results. In Fig. 5(a), the FE analytical results match the experimental results, and the initial stiffness is also in good agreement before the external load reached 130 kN; thereafter, the FE analytical stiffness is slightly larger than the experimental version, and the experimental curve is smoother than the FE one, because of the out-of-plane instability of the test specimens. The maximum test load was 437.7 kN, and the maximum FE analytical load was 446.1 kN. Fig. 5(b) shows that simulated and experimented results are in good agreement with each other, however the instability occurred earlier in the FE model.

Figure 6 shows the deformation of the two test specimens. The failure mode of finite element simulation traces the experimental result very well except for the shear buckling deformation location of the corrugated steel plate damper. The main reasons for the deviation are considered as the initial geometric imperfection and the material inhomogeneity of experimental specimens. It can be inferred that the FE analytical results of the corrugated steel plate damper are reasonable and effective. Accordingly, the current numerical analysis, results demonstrate that the FE model can predict the structural strength of the corrugated models as well as the failure modes thereof.

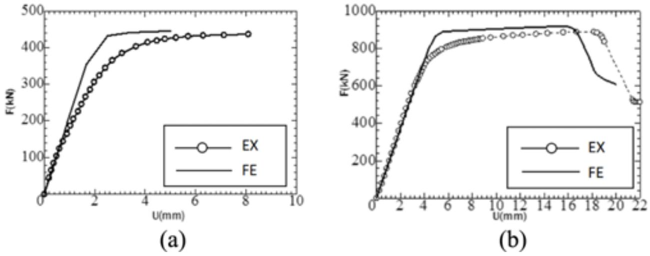

Fig. 5. Comparison of Load-Displacement Curves between Experiment and Finite Element Analysis: (a) CG240-0, (b) CG240-6

4. Mechanical Performance of the CSPD

4.1 Establishment of the CSPD Models

In this study, 25 finite element models were established to ascertain the effects of five parameters: ripple angle θ, width to thickness ratio of corrugated webs a_2/t_w, the number of corrugations n, the height to width ratio of the corrugated web H/B, and the ratio of the slanting segment to the straight segment a_1/a_2 of the plate on the mechanical properties and hysteresis behaviour of the CSPD. The model names take the form "CSPDθ-$a2/tw$-n-H/B-$a1/a2$", where CSPD represents the corrugated steel plate damper and θ-a_2/t_w-n-H/B-a_1/a_2 is the value of the letter (symbol). The thickness of the corrugated steel web (t_w) is 8 mm, the width (b_f) and the thickness (t_f) of the flange are 180 mm and 20 mm, respectively, and the length (L_f) and width (B_f) of the upper and lower flanges are 1,600 mm and

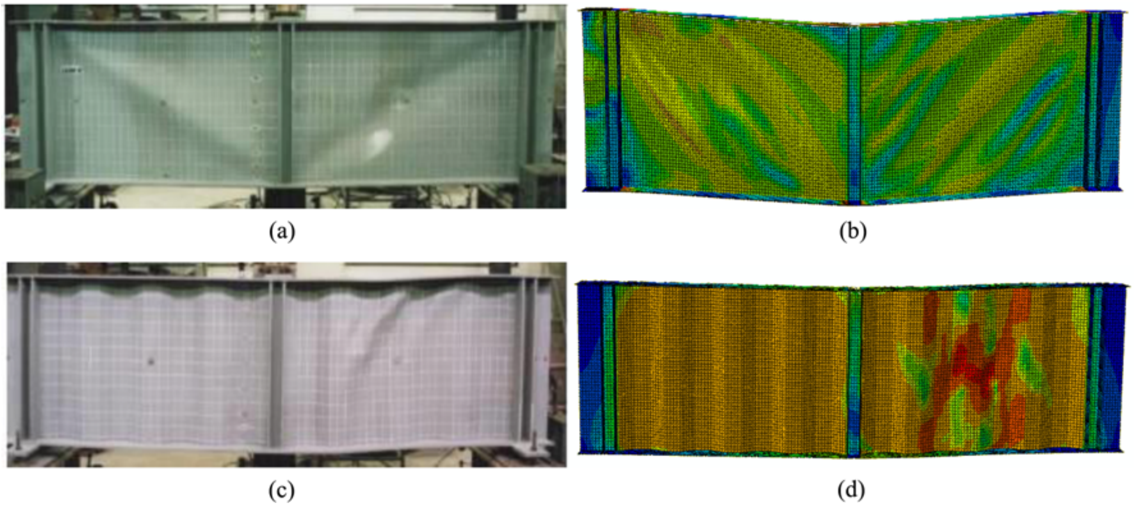

Fig. 6. Comparison of Experimental and Finite Element Analysis Data: (a) CG240-0 EX, (b) CG240-0 FE, (c) CG240-4 EX, (d) CG240-4 FE

Table 3. Geometric Parameters of the CSPD Model

Model	θ	a_2/t_w	n	H/B	a_1/a_2	F_y / kN	δ_y / mm	Model	θ	a_2/t_w	n	H/B	a_1/a_2	F_y / kN	δ_y / mm
CSPD$_{25\text{-}10\text{-}2\text{-}1\text{-}1}$	25°	10	2	1	1	865.2	1.37	CSPD$_{25\text{-}20\text{-}2\text{-}1\text{-}1}$	25°	20	2	1	1	1730.4	2.73
CSPD$_{30\text{-}10\text{-}2\text{-}1\text{-}1}$	30°	10				849.1	1.34	CSPD$_{30\text{-}20\text{-}2\text{-}1\text{-}1}$	30°	20				1698.2	2.68
CSPD$_{35\text{-}10\text{-}2\text{-}1\text{-}1}$	35°	10				830.2	1.31	CSPD$_{35\text{-}20\text{-}2\text{-}1\text{-}1}$	35°	20				1660.5	2.62
CSPD$_{40\text{-}10\text{-}2\text{-}1\text{-}1}$	40°	10				808.9	1.28	CSPD$_{40\text{-}20\text{-}2\text{-}1\text{-}1}$	40°	20				1617.8	2.56
CSPD$_{45\text{-}10\text{-}2\text{-}1\text{-}1}$	45°	10				785.3	1.24	CSPD$_{45\text{-}20\text{-}2\text{-}1\text{-}1}$	45°	20				1570.6	2.48
CSPD$_{25\text{-}15\text{-}2\text{-}1\text{-}1}$	25°	15	2	1	1	1297.8	2.06	CSPD$_{35\text{-}10\text{-}2\text{-}0.7\text{-}1}$	35°	10	2	0.7	1	830.2	0.92
CSPD$_{30\text{-}15\text{-}2\text{-}1\text{-}1}$	30°	15				1273.6	2.01	CSPD$_{30\text{-}15\text{-}2\text{-}0.7\text{-}1}$	30°	15	2	0.7	1	1273.6	1.41
CSPD$_{35\text{-}15\text{-}2\text{-}1\text{-}1}$	35°	15				1245.4	1.97	CSPD$_{25\text{-}20\text{-}2\text{-}0.7\text{-}1}$	25°	20	2	0.7	1	1730.4	1.91
CSPD$_{40\text{-}15\text{-}2\text{-}1\text{-}1}$	40°	15				1213.4	1.92	CSPD$_{45\text{-}10\text{-}2\text{-}1\text{-}0.5}$	45°	10	2	1	0.5	643.4	1.02
CSPD$_{45\text{-}15\text{-}2\text{-}1\text{-}1}$	45°	15				1177.9	1.86	CSPD$_{45\text{-}10\text{-}2\text{-}1\text{-}1}$					1	785.3	1.24
CSPD$_{25\text{-}20\text{-}4\text{-}1\text{-}1}$	25°	20	4	1	1	3260.2	5.14	CSPD$_{45\text{-}10\text{-}2\text{-}1\text{-}1.5}$					1.5	927.2	1.46
CSPD$_{30\text{-}15\text{-}4\text{-}1\text{-}1}$	30°	15	4	1	1	2396.7	3.78	CSPD$_{45\text{-}10\text{-}2\text{-}1\text{-}2}$					2	1069.0	1.69
CSPD$_{35\text{-}10\text{-}4\text{-}1\text{-}1}$	35°	10	4	1	1	1560.2	2.46								

Table 4. Mechanical Properties of the Materials

Material	Density (kg/m^3)	Elastic modulus (GPa)	Possion's ratio	Yield stress (MPa)	Ultimate stress (MPa)	Ultimate strain
SS400	7,800	206	0.3	235	358	0.06
SM490	7,800	206	0.3	355	495	0.06

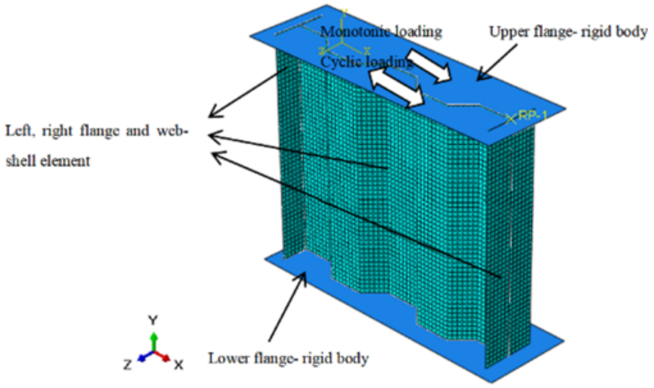

Fig. 7. Finite Element Model of Corrugated Plate Dampers

40 mm, respectively (key geometric parameters are listed in Table 3).

The shell element (S4R, four-node reduction integration element) was used to simulate corrugated steel webs and left and right flange plates, because the deformation and stress of the upper and lower flange plates are not the focus in the study, the upper and lower flange plates are considered as geometric rigid bodies in the model. The corrugated steel web was connected to the left and right flange plates by use of the Merge function. The bottom flange was subjected to a completely fixed constraint, the upper flange was coupled with the established reference point, and the constraints in all directions except the load direction were added at the reference point. The FE model is shown in Fig. 7.

The corrugated steel web, and left and right flange plates are made of SS400 and SM490 grade steel, respectively, for which a kinematic hardening model was adopted. The mechanical properties of the material are summarised in Table 4. The displacement load was applied at the reference point of the upper end during simulation. Monotonic load simulations were subjected to the static elasto-plastic analysis, and the maximum displacement of the load is 50 mm.

4.2 Mechanical Properties of the CSPD Model under Monotonic Loading

The load-displacement curves of the CSPD models under monotonic loading are shown in Fig. 8 which were used to analyse the effect of the five parameters on the mechanical properties of the CSPD. It was found that, although the initial stiffness and ultimate strength of CSPD increase slightly with increasing angle, the effect of angle on mechanical properties is not obvious. All of the five models have good mechanical properties, except for the model with an angle value of 25°, for which the bearing strength of the model decreases in the later loading stage (Fig. 8(a)). The initial stiffness, yield strength, and ultimate strength decrease with the increase of parameter a_1/a_2 (Fig. 8(b)). Comparing the result of the model with $H/B = 0.7$, when models suffer instability failure, the initial stiffness and ultimate strength of the model with $H/B = 1$ will be larger and the buckling will occur later, which indicates that the model with $H/B = 0.7$ is an optimal option (Fig. 8(c)). As shown in Fig. 8(d), with a_2/t_w increasing, the yield strength and ductility decrease, which indicates that the CSPD with $a_2/t_w = 10$ is optimal in this regard. The effect of parameter n on the mechanical properties is depicted in Fig. 8(e). A sudden decrease in strength and buckling failure was observed when $n = 4$ in these three groups of models ($n = 2$ is deemed optimal).

Figure 9 shows the displacement and von Mises stress contours of the four models at a displacement of 50 mm. Except for CSPD45-10-2-1-1, obvious buckling ripples were observed for specimens CSPD25-10-2-1-1, CSPD25-20-2-0.7-1, and CSPD25-20-4-1-1. The results indicate that the CSPD can restrain the buckling of steel webs when key parameters are within a certain range.

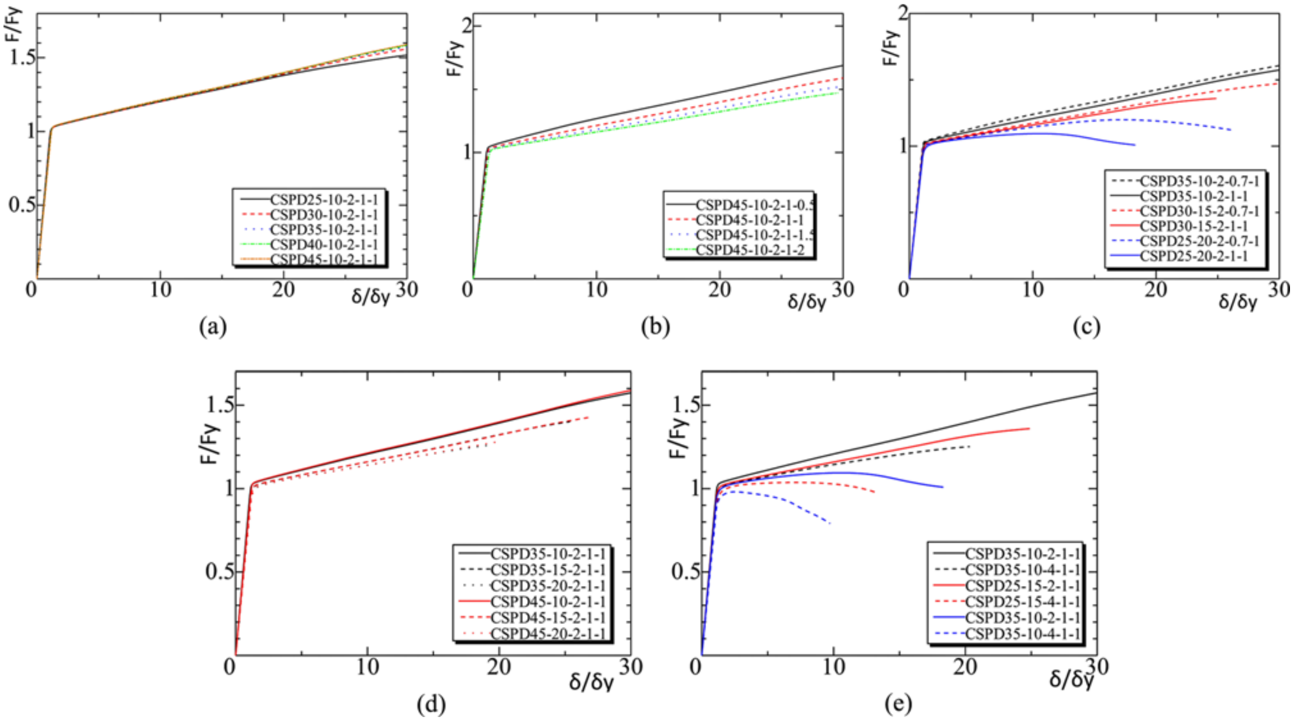

(a) (b) (c)

(d) (e)

Fig. 8. Load-Displacement Curves of CSPD under Monotonic Loading: (a) Parameter θ, (b) Parameter a_1/a_2, (c) Parameter H/B, (d) Parameter a_2/t_w, (e) Parameter n

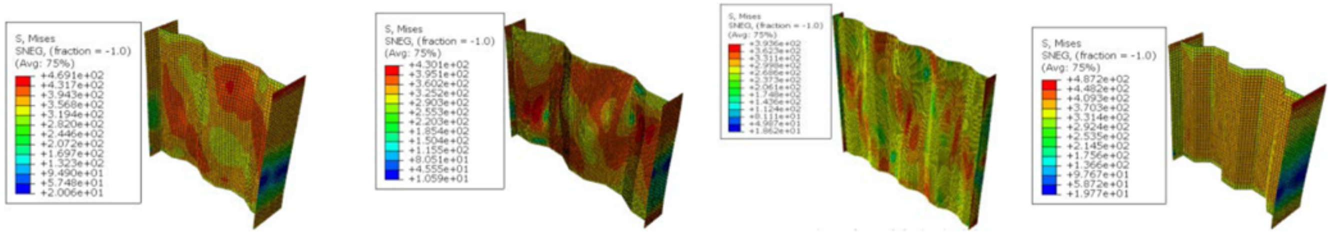

(a) (b) (c) (d)

Fig. 9. Stress Pattern and Deformation of CSPD at a Displacement of 50 mm (stress unit: MPa): (a) CSPD25-10-2-1-1, (b) CSPD25-20-2-0.7-1, (c) CSPD25-20-4-1-1, (d) CSPD45-10-2-1-1

4.3 Hysteretic Performance of the CSPDs

For quasi-static analysis, the models were loaded as shown in Fig. 10, and each cycle increment is 1.0 δ/δ_y.

Figure 11 shows the load-displacement hysteretic curves of CSPD30 – 45-10-2-1-1 under the cyclic loading protocol. The hysteretic curves of the four models are full, however, compared with the results showing that the strength increased continuously under monotonic load, the strength of CSPD30-10-2-1-1 began to deteriorate after the 12th loading step (corresponding displacement, 16.8 mm) (Fig. 11(a)). This is also seen in specimen CSPD35-10-2-1-1, however for specimens CSPD40-10-2-1-1 and CSPD45-10-2-1-1 (Figs. 11(b), 11(c), 11(d)), the hysteretic performance of the models improves with increasing angle and the hysteretic skeleton curves of all the models are compared in Fig. 12. It is indicated that parameter θ has little effect on the hysteretic performance and the bearing capacity increases monotonically, with no strength decreases seen at a ripple angle of 45 degrees (Fig. 12(a)). In Fig. 12(b), all three CSPDs may be seen to have offered good energy dissipation performances. When a_1/a_2 is 0.5 and 1.5, the strength decreases, as evinced by the hysteretic curve, is significant, the bearing capacity of the CSPD is degraded and the energy dissipation

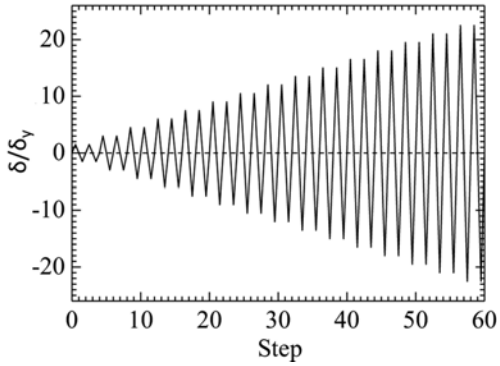

Fig. 10. Horizontal Cyclic Loading Protocol

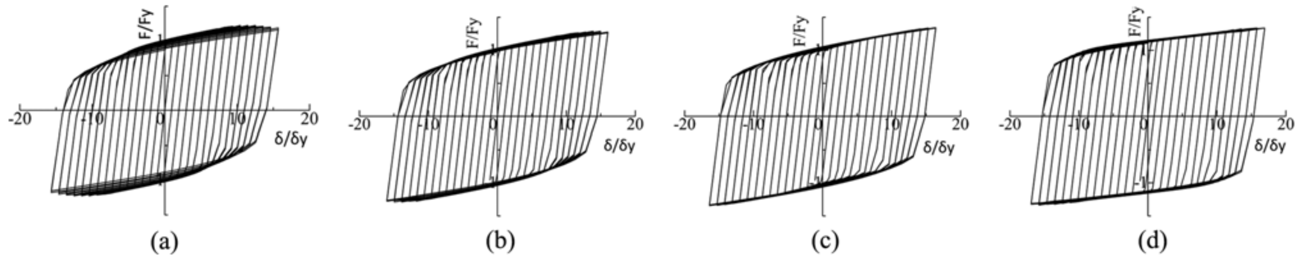

Fig. 11. Load-Displacement Hysteretic Curves of CSPD30 – 45-10-2-1-1: (a) CSPD30-10-2-1-1, (b) CSPD35-10-2-1-1, (c) CSPD40-10-2-1-1, (d) CSPD45-10-2-1-1

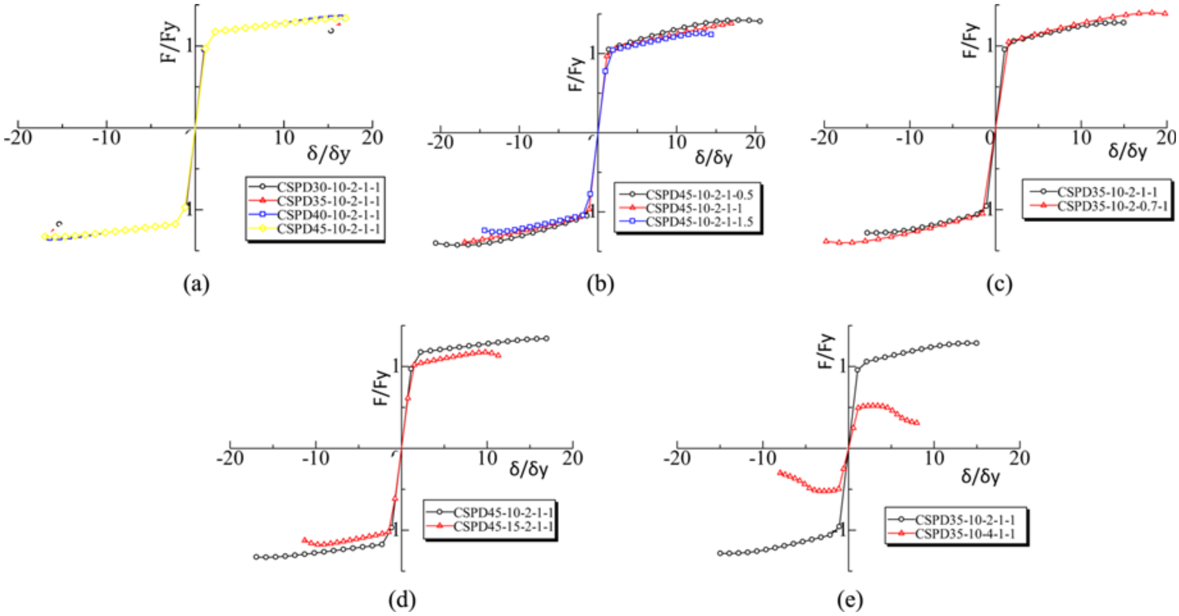

Fig. 12. Load-Displacement Hysteretic Skeleton Curves of CSPD under Cyclic Loading: (a) Parameter *θ*, (b) Parameter a_1/a_2, (c) Parameter *H/B*, (d) Parameter a_2/t_w, (e) Parameter *n*

performance becomes unstable: comparing the load-displacement curves at $H/B = 1.0$ and 0.7, the strength is slightly higher and will decrease under subsequent loading (Fig. 12(c)). Considering the ratio of a_2/t_w, when the ratio of width to thickness is 10, the hysteretic curve of the CSPD is full, and the strength tends to increase (Fig. 12(d)). As for design parameter *n*, it was found that at $n = 2$ a better hysteretic performance ensured than at $n = 4$, because the strength of specimens with $n = 4$ decreases significantly under load (Fig. 12(e)).

4.4 Simplified Constitutive Model of the CSPD

To make the CSPD more convenient when being applied in engineering practice, a simplified constitutive model was obtained which can accurately reflect the hysteresis performance.

Figure 12 indicates that the load-displacement curve is a bi-linear curve. According to Eqs. (2) and (3), the shear yield bearing capacity F_y (kN) and stiffness K_1 (kN/mm) for the constitutive model of a CSPD can be obtained, and then a fitting equation for the stiffness K_2 (kN/mm) in the plastic stage is proposed. According to Eq. (2), the stiffness K_2 can be calculated using a different formula related to parameter *B* when the ripple angle of the CSPD exceeds 25 degrees.

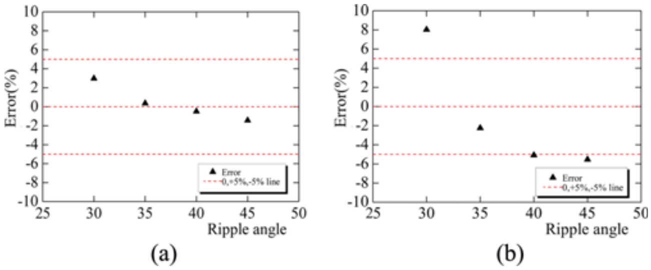

Fig. 13. Error Range Plots: (a) CSPD-10-2-1-1 (600 mm < B < 900 mm), (b) CSPD*θ*-20-2-1-1 (900 mm ≤ B < 1400 mm)

$$K_2=\left\{\begin{matrix} 0.0185K_1 & (600\,\mathrm{mm}<B<900\,\mathrm{mm}) \\ 0.0140K_1 & (900\,\mathrm{mm}\le B<1400\,\mathrm{mm}) \end{matrix}\right\} \tag{4}$$

The errors in the ratio of the theoretical formula calculation results and the finite element analysis result are shown in Fig. 13: all of the stiffness K_2 ratio errors are within 10%. Fig. 14 shows that the load-displacement curves obtained from the simplified constitutive model are consistent with the analytical results, which indicate that the bi-linear simplified model can be used to describe the mechanical performance of a CSPD.

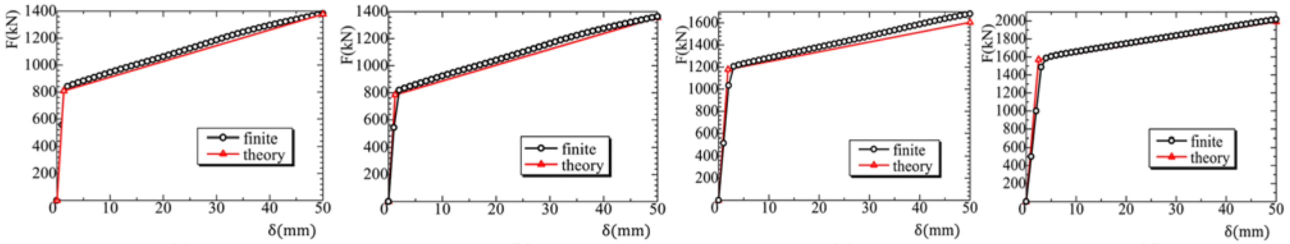

(a) (b) (c) (d)

Fig. 14. Comparison of the Results of a Simplified Bi-linear Model and the FE Analysis: (a) CSPD40-10-2-1-1, (b) CSPD45-10-2-1-1, (c) CSPD45-15-2-1-1, (d) CSPD45-20-2-1-1

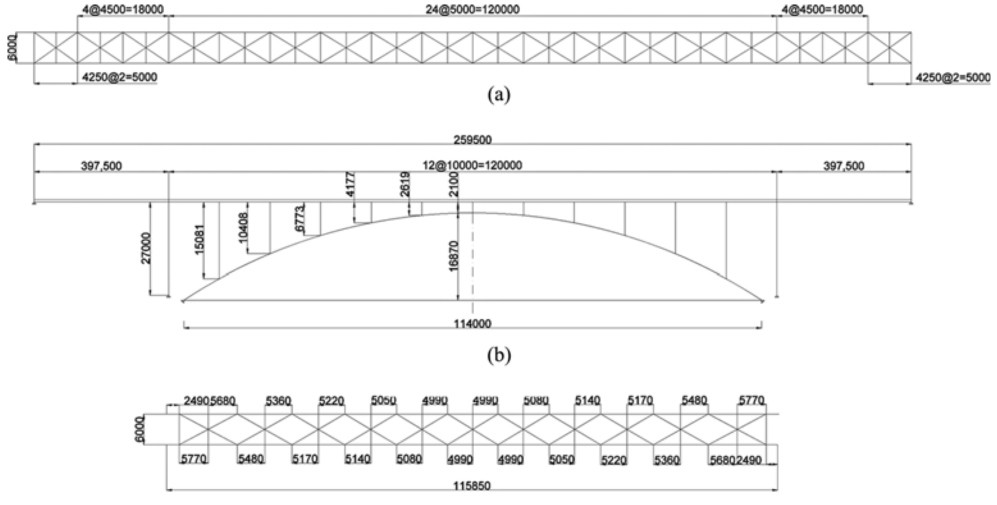

(c)

Fig. 15. Structural Layout of the Arch Bridge (unit: mm): (a) Top View, (b) Elevation, (c) Top View Arch Rib

Table 5. Geometric Parameters of the Applied Damper

Specification	θ	a_1 (mm)	a_2 (mm)	t_w (mm)	t_f (mm)	b_f (mm)	B (mm)	H (mm)	F_y (kN)	δ_y (mm)
CSPD45-10-2-0.7-1	45	80	80	8	20	180	626	438	785.3	0.89

5. Application to a Steel Arch Bridge

5.1 Profile of the Steel Arch Bridge

Figure 15 shows the structural layout of the upper-deck type steel truss arch bridge. The upper-deck type steel truss arch bridge is composed of the bridge deck, I-shaped longitudinal beam, box pier, and single span steel arch rib with a box section. The total length of the bridge is 173 m. The span and height of the arch rib are 114 m and 16.87 m, respectively (so the span to height ratio is 1:6.76). Two sides of the arch rib are connected by transverse braces. The cross-beams and the top braces are set between the two main beams and the two columns which are symmetrical in the longitudinal direction. The arch rib is a box section, the side pier is a square section, and the steel beam is formed from an I-shaped section. The reinforced concrete deck is of rectangular section, and the concrete pavement is 8.2 m wide and 0.22 m thick (Usami et al., 2004; Lu et al., 2004). The bridge is built in an area of high seismic intensity (Ground Type II).

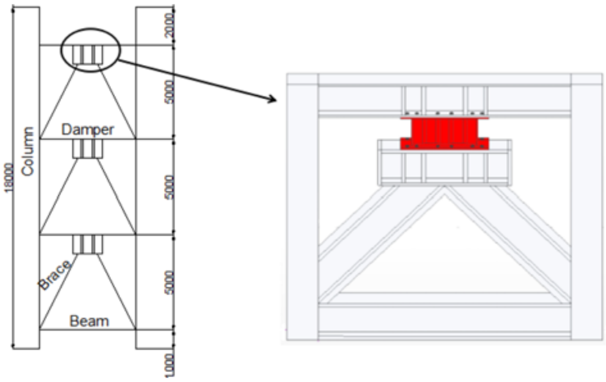

Fig. 16. Installation of the CSPD

According to the available analytical results, it was found that the weakest position was around the side piers, so the CSPDs, with their better mechanical properties according to the analytical results, were applied on the side piers of the upper-deck type steel arch bridge to reveal the influence of CSPD on seismic performance. The geometric parameters and installation instruction of CSPD are as shown in Table 5 and Fig. 16.

The arch bridges without, and with, the CSPD are referred to as the "Original arch bridge" and "Arch bridge-CSPD" respectively. SM490 steel was used for all beams, diagonal bracing between beams, arch ribs, diagonal bracing between arch ribs, side piers, and diagonal and cross-bracing between side piers; SS400 was used for cross-bracing between two beams, columns, cross and diagonal bracing between two columns or arch vault, and diagonal bracing between the two arch ribs.

5.2 Analytical model of "Original Arch Bridge" and "Arch Bridge-CSPD"

This section describes the establishment of the finite element analysis model of the arch bridge. Shell element (S4R) was employed to simulate the bridge deck, and beam element (B31) was used to simulate the longitudinal beam, the column, the arch rib, the transverse bracing, and the inclined bracing. Truss element T3D2 was used to simulate the CSPD and the simplified constitutive model, stiffness equivalence principle, and Hooke's law were used to establish the mechanical properties and cross-sectional area of the truss element (Chen et al., 2011; Li et al., 2016; Li et al., 2017). The models are shown in Fig. 17.

The contact and boundary conditions of models are as follows: the bridge deck and the beam are connected by tie members, the side piers and the beams are connected by rigid connection, and the columns are connected with the beams and the arch ribs by hinges. The boundary conditions of the models are summarised in Table 6.

Table 6. Boundary Conditions

Position	X	Y	Z	UR1	UR2	UR3
P1, P2, P3, P4	Free	Fixed	Fixed	Free	Free	Free
P5, P6, P7, P8	Fixed	Fixed	Fixed	Fixed	Free	Fixed
P9, P10, P11, P12	Fixed	Fixed	Fixed	Free	Free	Free

Note: X-longitudinal direction of bridge, Y-vertical direction of bridge, *Z*-transverse direction of bridge, UR1 *X*-axis rotation direction, UR2 *Y*-axis rotation direction, UR3 *Z*-axis rotation direction

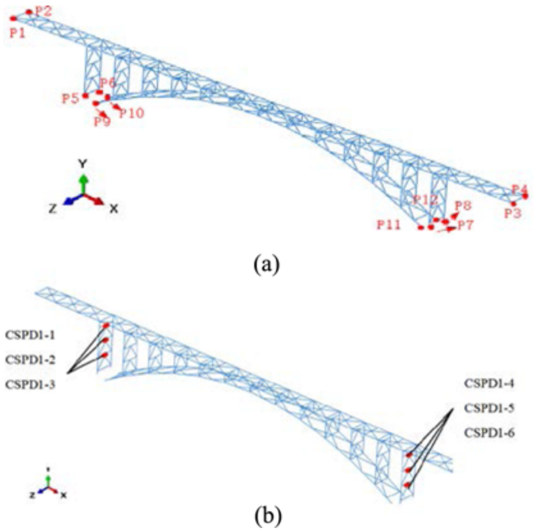

Fig. 17. Finite Element Models of the Upper-Deck Type Steel Truss Arch Bridge: (a) Original Arch Bridge, (b) Arch Bridge-CSPD

5.3 Eigenvalue Analysis

Eigenvalue analysis was carried out to explicit the dynamic characteristics of the arch bridge. The natural period and effective mass ratio of the first twelve modes of the bridge are listed in Table 7, and typical modes of the arch bridge (modes 1, 2, 6, and 11) are shown in Fig. 18.

The period of the first mode of the "original arch bridge" is the longest at 1.321 s. The maximum value of the effective mass ratios in longitudinal, vertical, and transverse directions appear in the eleventh, sixth, and second modes, respectively

Table 7. Eigenvalue Results

Original arch bridge					Arch bridge-CSPD				
Mode	Period, T (s)	Effective mass ratio			Mode	Period, T (s)	Effective mass ratio		
		β_x	β_y	β_z			β_x	β_y	β_z
1	**1.321**	**18.1%**	**0.0%**	**0.0%**	**1**	**1.233**	**17.71%**	**0.0%**	**0.0%**
2	**0.842**	**0.0%**	**0.0%**	**71.4%**	**2**	**0.796**	**0.0%**	**0.0%**	**69.53%**
3	0.578	0.0%	0.6%	0.0%	3	0.571	0.0%	0.55%	0.0%
4	0.413	0.0%	0.0%	0.0%	4	0.383	0.0%	0.0%	0.0%
5	0.349	10.1%	0.0%	0.0%	5	0.341	9.39%	0.01%	0.0%
6	**0.320**	**0.0%**	**50.1%**	**0.0%**	**6**	**0.319**	**0.0%**	**51.3%**	**0.0%**
7	0.264	0.0%	18.9%	0.0%	7	0.260	0.0%	19.33%	0.0%
8	0.258	11.7%	0.0%	0.0%	8	0.251	6.22%	0.0%	0.0%
9	0.255	0.0%	0.0%	2.8%	9	0.248	0.01%	0.0%	0.41%
10	0.236	0.0%	0.0%	12.1%	10	0.230	0.0%	0.0%	15.61%
11	0.212	47.3%	0.0%	0.0%	11	0.206	53.6%	0.0%	0.0%
12	0.198	0.0%	12.5%	0.0%	12	0.198	0.0%	11.35%	0.0%

Note: β_x, β_y, β_z = effective mass ratio of longitudinal direction, vertical direction, transverse direction, respectively.

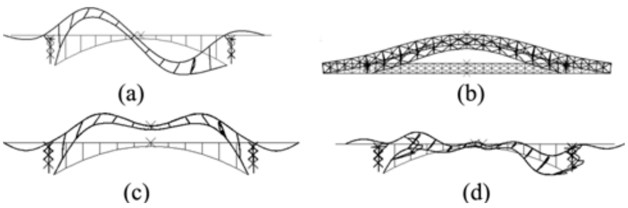

Fig. 18. Typical Modes of Vibration of the "Original Arch Bridge" (arch bridge-CSPD): (a) Mode 1 1.321 s (1.233 s), (b) Mode 2 0.842 s (0.796 s), (c) Mode 6 0.320 s (0.319 s), (d) Mode 11 0.212 s (0.206 s)

(corresponding values are 47.3%, 50.1%, and 71.4%, respectively).

As for the "arch bridge-CSPD", the longest period is 1.233 s, which occurs in the first mode. The maximum value of the effective mass ratios in longitudinal, vertical, and transverse directions appear in the eleventh, sixth, and second modes, respectively (corresponding values are 53.6%, 51.3%, and 69.53%, respectively). The period, effective mass ratio and form of vibration of "arch bridge-CSPD" are similar to those of the "original arch bridge", and both bridges meet seismic design criteria.

5.4 Dynamic Response Results

Dynamic time history analysis, using the Newmark-β method (β = 0.25), was undertaken to study the effect of the CSPDs on seismic response of the arch bridge. For the dynamic analyses, a two-step loading is adopted, i.e,, first the dead load is applied and then it is subject to ground motion input. An automatic increment with a maximum of 0.01 s is set. The JTR-NS, JRT-EW, OGF-N27W accelerogram were input with the peak ground accelerations (PGA) of 0.70 g, 0.69 g, 0.75 g, respectively. Three seismic waves with 30s duration were modified seismic records obtained from the 1995 Kobe earthquake (Fig. 19).

The specific peak displacement of arch bridge under the three ground motions is listed in Table 8. The displacement response of JRT-NS at ¼-span of the arch rib, vault and middle of arch is slightly larger than that under the other ground motions: the installation of the CSPD can attenuate the displacement response at key sections of this arch bridge.

The displacement response, axial response, and strain curve of the "original arch bridge" and "arch bridge-CSPD" under JRT-NS motion were obtained. The transverse and vertical displacement responses of the "arch bridge-CSPD" are significantly

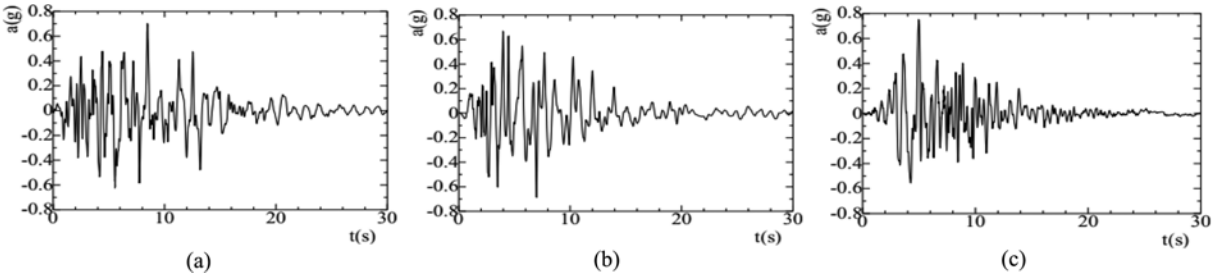

Fig. 19. Three Seismic Wave Records: (a) JRT-NS, (b) JRT-EW, (c) OGF-N27W

Table 8. Peak Displacement of the Arch Bridge

Ground motion	Section	Direction	Original arch bridge (m)	Arch bridge-CSPD (m)	Difference ratio
JRT-NS	¼-arch rib	Transverse	0.301	0.192	-36.2%
		Vertical	0.093	0.063	-32.26%
	Vault of arch	Transverse	0.468	0.321	-31.41%
		Vertical	0.109	0.087	-20.18%
	Middle of arch	Transverse	0.530	0.368	-30.57%
		Vertical	0.110	0.087	-20.91%
JRT-EW	¼-arch rib	Transverse	0.243	0.189	-22.22%
		Vertical	0.084	0.055	-34.52%
	Vault of arch	Transverse	0.403	0.333	-17.37%
		Vertical	0.116	0.075	-35.34%
	Middle of arch	Transverse	0.470	0.393	-16.38%
		Vertical	0.117	0.075	-35.90%
OGF-N27W	¼-arch rib	Transverse	0.272	0.224	-17.65%
		Vertical	0.084	0.070	-16.67%
	Vault of arch	Transverse	0.427	0.374	-12.41%
		Vertical	0.106	0.101	-4.72%
	Middle of arch	Transverse	0.488	0.435	-10.86%
		Vertical	0.107	0.102	-4.67%

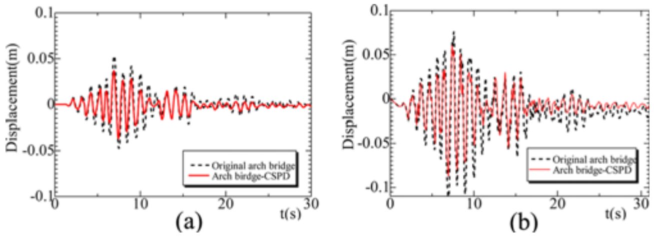

Fig. 20. Time History Curves of Mid-span Displacement of Longitudinal Girder under JRT-NS Motion: (a) Transverse Displacement Time History Curve, (b) Vertical Displacement Time History Curve

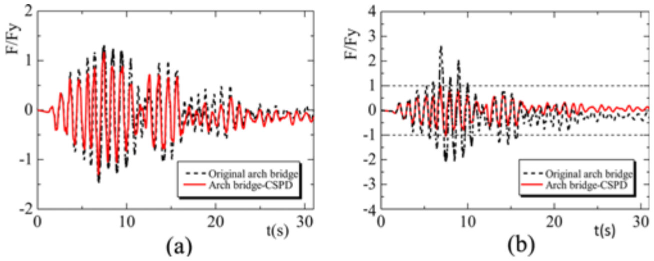

Fig. 21. Axial Force and Strain Time History: Side Pier Base under JRT-NS Motion: (a) Axial Force Time History Curve, (b) Strain Time History Curve

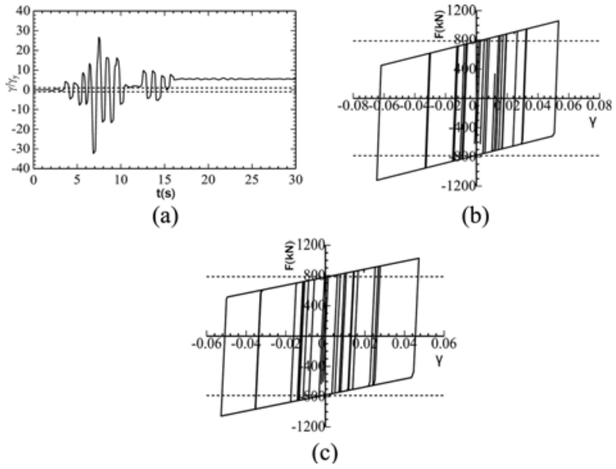

Fig. 22. Hysteretic and Strain Time History Curves of the Corrugated Plate Damper: (a) CWD1-3 Strain Time History Curve, (b) CWD1-3 Load-Strain Curve, (c) CWD1-5 Load-Strain Curve

smaller than those of the "original arch bridge". Among them, at 7.4 s, the maximum transverse displacement of the "arch bridge - CSPD" is 0.368 m, which is 30.57% less than the maximum displacement of the original arch bridge (0.53 m, Fig. 20(a)). The axial force of "arch bridge-CSPD" is smaller than that of "original arch bridge". The maximum axial force of "original arch bridge" was reduced 13.9% by adopting CSPD (Fig. 21(a)). The bottom of the side piers of "Arch bridge-CSPD" is subjected to elastic deformation, while the bottom of the side piers without dampers undergoes plastic deformation after 3 s, which indicates that the application of the CSPD reduces the damage to the arch bridge under transverse ground motion (Fig. 21(b)).

According to the results of hysteretic and non-dimensional shear displacement time history curves of the CSPD (Fig. 22), the CSPD enters the plastic deformation stage at 3 s, and the maximum shear displacement is 32 times the shear yield displacement, which indicated that the CSPD provided a high energy dissipation capacity and could reduce the damage to such an arch bridge under ground motion.

6. Conclusions

1. The stiffness and ductility of the corrugated steel plates increase with increasing ripple angle, and the ideal ripple angle range is from 35 to 45 degrees. The stiffness and ductility of the corrugated steel webs decrease with increasing height to width ratio, the ratio of inclined plate to straight section, and the number of corrugations. The design range of the height to width ratio is between 0.7 and 1.0.
2. The CSPD exhibits good hysteretic behaviour under reasonable geometric design parameters. The hysteretic performance of the CSPD tends to become more stable as the ripple angle increases. The CSPD with the slanting plate to straight plate ratio of 1 has good hysteretic behaviour and convenient production. The ripple number should be two. If a single CSPD cannot meet the force requirements, the number of CSPD can be raised.
3. Under transverse earthquake motion, the layout of the CSPD can reduce the seismic response of an upper-deck-type steel truss arch bridge. Compared with the original arch bridge, the lateral and vertical displacement responses of an arch bridge with a corrugated steel plate damper are decreased by 31.41% and 20.18%, respectively.
4. The deviation of analysis results using the FE analysis model can guarantee the accuracy required by engineering application, which prove that the FE analysis model can be used to simulate the mechanical properties of CSPD and the seismic performance of arch bridge under strong ground motions. However, the simulation of the shear buckling deformation of CSPD should be studied further.

Acknowledgements

This study was supported by the Project of the National Science and Technology Ministry 13th Five-Year Science and Technology (2018YFC0809606-03), the supports is gratefully acknowledged.

ORCID

Not Applicable

References

Abbas HH, Sause R, Driver RG (2007a) Analysis of flange transverse bending of corrugated web I-girders under in-plane loads. *Journal of Structural Engineering* 133(3):347-355, DOI: 10.1061/(ASCE)

0733-9445(2007)133:3(347)

Abbas HH, Sause R, Driver RG (2007b) Simplified analysis of flange transverse bending of corrugated web I-girders under in-plane moment and shear. *Engineering Structures* 29(11):2816-2824, DOI: 10.1016/j.engstruct.2007.01.006

AISC 341-10 (2010) Seismic provisions for structural steel buildings. ANSI/AISC 341-10, Chicago, IL, USA

Anish KA, Chakrabarti A (2019a) Failure mode analysis of laminated composite sandwich plate. *Engineering Failure Analysis* 104:950-976, DOI: 10.1016/j.engfailanal.2019.06.080

Anish CA, Kumar A, Kwiatkowski B, Barnat-Hunek D, Widomski MK (2019b) Bi-axial buckling of laminated composite plates including cutout and additional mass. *Materials* 12(11):1750, DOI: 10.3390/ma12111750

Anish CA, Vishwakarma S, Kumar A, Fic S, Barnat-Hunek D (2019c) Transient response of rhombic laminates. *Structure Engineering and Mechanics* 70(5):551-562, DOI: 10.12989/sem.2019.70.5.551

Ansari MI, Kumar A (2019) Flexural analysis of functionally graded CNT-reinforced doubly curved singly ruled composite truncated cone. *Journal of Aerospace Engineering* 32(2):04018154, DOI: 10.1061/(asce)as.1943-5525.0000988

Bruneau M (1998) Performance of steel bridges during the 1995 Hyogoken–Nanbu (Kobe, Japan) earthquake - A North American perspective. *Engineering Structures* 20(12):1063-1078, DOI: 10.1016/s0141-0296(97)00203-4

Chaubey AK, Jha I, Kumar A, Demirbas MD, Dey S (2018b) Dual-axis buckling of laminated composite skew hyperbolic paraboloids with openings. *Journal of the Brazilian Society of Mechanical Sciences and Engineering* 40(10), DOI: 10.1007/s40430-018-1406-z

Chaubey AK, Prakash C, Kumar A (2018a) Biaxial and shear buckling of laminated composite elliptic paraboloids with cutouts and concentrated mass. *Mechanics Research Communications* 94:80-87, DOI: 10.1016/j.mechrescom.2018.09.008

Chen ZY, Ge HB, Usami T (2006) Hysteretic model of stiffened shear panel dampers. *JSCE Journal of Structural Engineering* 132(3):478-483, DOI: 10.1016/B978-008044637-0/50181-5

Chen X, Ge HB, Usami T (2011) Seismic demand of buckling-restrained braces installed in steel arch bridges under repeated earthquakes. *Journal of Earthquake and Tsunami* 5(2):119-150, DOI: 10.1142/S1793431111000942

CSA (2009) Limit states design of steel structures. CAN/CSA S16-2009, Canadian Standard Association, Mississauga, ON, Canada

Deng WQ, Liu D, Xiu YQ, Zhang JD (2019) Experimental study on asynchronous construction for composite bridges with corrugated steel webs. *Journal of Constructional Steel Research* 157(2019):93-102, DOI: 10.1016/j.jcsr.2019.02.028

Dou C, Pi YL, Gao W (2018) Shear resistance and post-buckling behavior of corrugated panels in steel plate shear walls. *Thin-Walled Structures* 131(10):816-826, DOI: 10.1016/j.tws.2018.07.039

Du XL, Han Q, Li ZX, Li LY, Chen SF, Zhang JF (2008) The seismic damage of bridges in the 2008 Wenchuan earthquake and lessons from its damage. *Journal of Beijing University of Technology* 34(12):1270-1279, DOI: 10.11936/bjutxb2008121270

Elkawas AA, Hassanein MF, El-Boghdadi MH (2017) Numerical investigation on the nonlinear shear behavior of high-strength steel tapered corrugated web bridge girders. *Engineering Structures* 134(2017):358-375, DOI: 10.1016/j.engstruct.2016.12.044

EN 1993-1-5 Eurocode 3 (2005) Design of steel structures, part1 – 5: Plated structural elements. EN 1993-1-5-Eurocode3, European Committee for Standardization, Brussels, Belgium

Ezzeldin YS (2007) Design aspects of steel I-girders with corrugated steel webs. *Electronic Journal of Structural Engineering* 7:27-40

Farhad R, Alaeddin B, Mikaeil YF, Arastoo A (2018) Shear buckling analysis of steel flat and corrugated web I-girders. *KSCE Journal of Civil Engineering* 22(12):5058-5073, DOI: 10.1007/s12205-017-1530-9

Ibrahim SA, El-Dakhakhni WW, Elgaaly M (2006) Behavior of bridge girders with corrugated webs under monotonic and cyclic loading. *Engineering Structures* 28(14):1941-1955, DOI: 10.1016/j.engstruct.2006.03.026

Ichioka Y, Kono S, Nishiyama Y, Watanabe F (2009) Hybrid system using precast prestressed frame with corrugated steel panel damper. *Journal of Advanced Concrete Technology* 7(3):297-306, DOI: 10.3151/jact.7.297

Iemura H (2012) Seismic safety enhancement of long span bridges with base isolation and structural control technology. *JSCE Journal of Structural Engineering* 58A:1-16, DOI: 10.11532/structcivil. 58A.1

Jáger B, Dunai L, Kövesdi B (2015) Girders with trapezoidally corrugated webs subjected by combination of bending, shear and path loading. *Thin-Walled Structures* 96(96):27-239, DOI: 10.1016/j.tws.2015.08.015

Kalali H, Ghazijahani GT, Hajsadeghi M, Zirakian T, Alaee FJ (2016) Numerical study on steel shear walls with sinusoidal corrugated plates. *Latin American Journal of Solids and Structures* 13(15):2802-2814, DOI: 10.1590/1679-78252837

Kubo M, Watanabe K (2007) Lateral-torsional buckling capacity of steel girders with corrugated web plates. *JSCE Journal of Structural Engineering* 63(1):179-193, DOI: 10.2208/jsceja.63.179

Kumar A, Chakrabarti A, Bhargava P (2013) Vibration of laminated composites and sandwich shells based on higher order zigzag theory, *Engineering Structures* 56:880-888, DOI: 10.1016/j.engstruct.2013.06.014

Li R, Ge HB, Maruyama R (2017) Assessment of post-earthquake serviceability for steel arch bridges with seismic dampers considering main shock-aftershock sequences. *Earthquakes and Structures* 13(2):137-150, DOI: 10.12989/eas.2017.13.2.137

Li R, Ge HB, Usami T, Shu GP (2016) A strain-based post-earthquake serviceability verification method for steel frame-typed bridge piers installed with seismic dampers. *Journal of Earthquake Engineering* 21(4):635-651, DOI: 10.1080/13632469.2016.1157531

Lu Z, Usami T, Ge HB (2004) Seismic performance evaluation of steel arch bridges against major earthquakes. Part 2: Simplified verification procedure. *Earthquake Engineering & Structural Dynamics* 33(14):1355-1372, DOI: 10.1002/eqe.407

Machimdamrong C, Watanabe E, Utsunomiya T (2004) Analysis of corrugated steel web girders by an efficient beam bending theory. *Structural Engineering/Earthquake Engineering* 21(2):131s-142s, DOI: 10.2208/jsceseee.21.131s

Nakashima M (1995) Strain-hardening behavior of shear panels made of low-yield steel I: Test. *Journal of Structural Engineering* 121(12):1742-1749, DOI: 10.1061/(ASCE)0733-9445(1995)121:12(1742)

Nakashima M, Akazawa T, Tsuji B (1995) Strain-hardening behavior of shear panels made of low-yield steel. II: Model. *Journal of Structural Engineering* 121(12):1750-1757, DOI: 10.1061/(ASCE)0733-9445(1995)121:12(1750)

Qiu J, Zhao QH, Yu C, Li ZX (2018) Experimental studies on cyclic behavior of corrugated steel plate shear walls. *Journal of Structural Engineering* 144(11):04018200, DOI: 10.1061/(ASCE)st.1943-541x.0002165

SIMULIA (2013) ABAQUS standard manual, version 6.14. The Dassault Systèmes, Realistic Simulation, Providence, RI, USA

Tanaka K, Sasaki Y (2000) Hysteretic performance of shear panel dampers of ultra-low yield-strength steel for seismic response control of buildings. The 12th World Conference on Earthquake Engineering, New Zealand, 1248-1260

Usami T, Lu Z, Ge HB, Takeshi K (2004) Seismic performance evaluation of steel arch bridges against major earthquakes. Part 1: Dynamic analysis approach. *Earthquake Engineering & Structural Dynamics* 33(14):1337-1354, DOI: 10.1002/eqe.407

Usami T, Zheng Y, Ge HB (2000) Recent research developments in stability and ductility of steel bridge structures: General report. *Journal of Constructional Steel Research* 55:183-209, DOI: 10.1016/S0143-974X(99)00085-1

Wang KH, Han W, Li Q, Li Y (2012) Philosophies on seismic design of highway bridges of small or medium spans. *China Civil Engineering Journal* 45(9):115-121, DOI: 10.15951/j.tmgcxb.2012.09.012

Wang SH, Liu YQ, He J, Xin HH, Yan HB (2019) Experimental study on cyclic behavior of composite beam with corrugated steel web considering different shear-span ratio. *Engineering Structures* 180 (2019):669-684, DOI: 10.1016/j.engstruct.2018.11.044

Watanabe K, Kubo M (2006) In-plane bending capacity of steel girders with corrugated web plates. *JSCE Journal of Structural Engineering* 62(2):323-336, DOI: 10.2208/jsceja.62.323

Xu LY, Tao MX, Nie X, Fan JS, Taciroglu E (2017) Modeling techniques for strain-range dependent hardening behavior of low-yield-point steel shear panel dampers. *Journal of Structural Engineering* 143(12): 04017172(1-10), DOI: 10.1061/(ASCE)ST.1943-541X.0001896

Yi J, Gil H, Youm K, Lee H (2008) Interactive shear buckling behavior of trapezoidally corrugated steel webs. *Engineering Structures* 30(6):1659-1666, DOI: 10.1016/j.engstruct.2007.11.009

Zhang CF, Zhang ZS, Shi JF (2012) Development of high deformation capacity low yield strength steel shear panel damper, *Journal of Constructional Steel Research* 75(7):116-130, DOI: 10.1016/j.jcsr.2012.03.014